Feedback Analysis and Design of RF Power Links for Low-Power Bionic Systems

Michael W. Baker, *Student Member, IEEE*, and Rahul Sarpeshkar, *Member, IEEE*

Invited Paper

Abstract—**This paper presents a feedback-loop technique for analyzing and designing RF power links for transcutaneous bionic systems, i.e., between an external RF coil and an internal RF coil implanted inside the body. The feedback techniques shed geometric insight into link design and minimize algebraic manipulations. We demonstrate that when the loop transmission of the link's feedback loop is −1, the link is critically coupled, i.e., the magnitude of the voltage transfer function across the link is maximal. We also derive an optimal loading condition that maximizes the energy efficiency of the link and use it as a basis for our link design. We present an example of a bionic implant system designed for load power consumptions in the 1–10-mW range, a low-power regime not significantly explored in prior designs. Such low power levels add to the challenge of link efficiency, because the overhead associated with switching losses in power amplifiers at the link input and with rectifiers at the link output significantly degrade link efficiency. We describe a novel integrated Class-E power amplifier design that uses a simple control strategy to minimize such losses. At 10-mW load power consumption, we measure overall link efficiencies of 74% and 54% at 1- and 10-mm coil separations, respectively, in good agreement with our theoretical predictions of the link's efficiency. At 1-mW load power consumption, we measure link efficiencies of 67% and 51% at 1- and 10-mm coil separations, respectively, also in good accord with our theoretical predictions. In both cases, the link's rectified output dc voltage varied by less than 16% over link distances that ranged from 2 to 10 mm.**

Index Terms—**Biomedical power supplies, feedback systems, implantable biomedical devices, low-power systems, power transformer, RF powering, transcutaneous power transfer.**

I. INTRODUCTION

IMPLANTED electronics are used in medical devices for diagnosis as well as for treatment of a wide variety of conditions—pacemakers for cardiac arrhythmia, retinal implants for the blind, cochlear implants for deafness, deep-brain stimulators for Parkinson's disease, spinal-cord stimulators for control of pain, and brain-machine interfaces for paralysis prosthetics. Such devices need to be small and operate with low power to make chronic and portable medical implants possible. They are most often powered by inductive RF links to avoid the need for implanted batteries, which can potentially lose all their charge or necessitate resurgery if they need to be replaced. Even when such devices have implanted batteries, an increasing trend in upcoming fully implanted systems, wireless recharging of the battery through RF links is periodically necessary.

Fig. 1 shows the basic structure of an inductive power link system for an example implant. An RF power amplifier drives a primary RF coil which sends power inductively across the skin of the patient to a secondary RF coil. The RF signal on the secondary coil is rectified and used to create a power supply that powers internal signal-processing circuits, electrodes and electrode-control circuits, signal-sensing circuits, or telemetry circuits depending on the application. The power consumption of the implanted circuitry is eventually borne by external batteries that power the primary RF coil; if an RF link is energy efficient, most of the energy in the primary RF coil will be transported across the skin and dissipated in circuits in the secondary. It is also important for an RF link to be designed such that the power-supply voltage created in the secondary is relatively invariant to varying link distances between the primary and secondary, due to patient skin-flap-thickness variability, device-placement, and device variability.

Recent advances in signal processing and electrode design have reduced power dissipation in internal circuits considerably. For example, a cochlear implant processor with only 250 μW of signal-processing power [1], [2] can be combined with electrodes that dissipate 750 μW of power via lowered impedance strategies or low-power stimulation strategies [3] to create cochlear-implant systems that dissipate 1 mW of power. Pacemaker systems often run on power levels that range from 10 μW to 1 mW depending on their complexity. RF power links for such systems need to achieve good energy efficiency such that needless amounts of external power are not used to power an efficient internal system. This paper explores the design of such RF links and builds on prior work in relatively high-power systems. Small losses that are important in low-power systems, may be insignificant in higher-power systems. For example, the retinal-implant design described in [4] is geared towards systems that dissipate near 250 mW; it dissipates 40 mW in its closed-loop Class-E power amplifiers alone, which is prohibitive for our intended applications but acceptable in the retinal-implant design. As another example, the design described in [5] is geared towards a link system that is capable of driving amperes of current into the primary portion of the
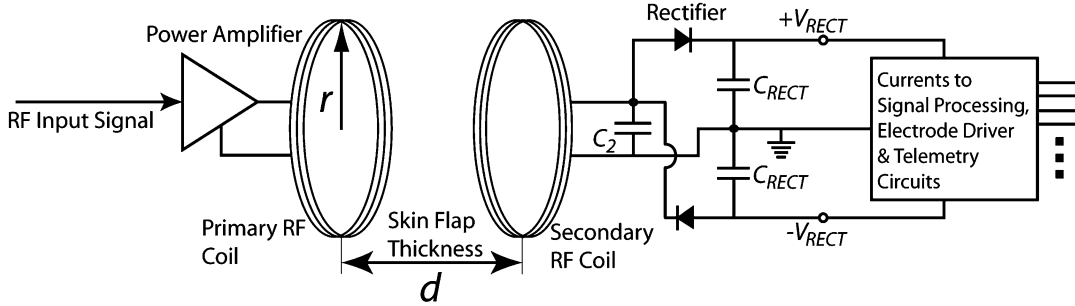
Fig. 1.   Example of a low-power bionic implant system is shown.

link such that a reasonable amount of power may be received in several tiny secondaries.

A theoretical model of RF links has been described in [6] who focused on operating at conditions of critical coupling. In critically coupled conditions, the magnitude of the voltage transfer function from the primary to the secondary is maximized and the voltage is relatively invariant to varying link distances. However, the energy-transfer efficiency has a theoretical maximum of 50% at critical coupling, and actual experimental measurements were found to be in 5%–32% range, lower than is desirable for our applications. In our work, we focus on designing for maximum link energy efficiency and obtain acceptable robustness to inter-coil separation. We derive an explicit loading condition for optimal energy efficiency and show that our measurements are in good accord with theory. Our feedback method yields a simple and pleasing result that shows that at critical coupling, the feedback-loop transmission is -1, a result in accord with formulas in [6].

The work in [7] describes a clever technique for adapting the operating frequency of a Class-E power amplifier such that good energy efficiency is always maintained independent of the geometry-dependent coupling between the primary and secondary. The technique appears to be more suited to relatively high coupling, requires a tapped primary, and measurements did not include efficiency losses due to rectifier circuits. We have chosen a simpler and different power-amplifier topology in this work to minimize power losses that may be caused by added complexity and to minimize robustness and instability issues caused by more complex Class-E topologies.

We shall only focus on issues regarding power transfer since efficient power transfer is the bottle neck in RF links, not efficient data transfer. Several other papers have described schemes for sending power and data through the same link [5], [8], [9]. It is worth pointing out that power transfer is more efficient with high-Q coils, a requirement that can conflict with data transfer if a high bandwidth data link is necessary. Thus, it is often advantageous to optimize power and data transfer at different operating frequencies.

The contributions of this paper are twofold. First, we describe a feedback analysis which aides in understanding optimal voltage-transfer and power-transfer functions for coupled resonators from a viewpoint that appears to be simpler than prior algebraic analyses and leads to a methodology for systematic design. Second, we describe the design of a low-power integrated Class-E power amplifier switch and controller
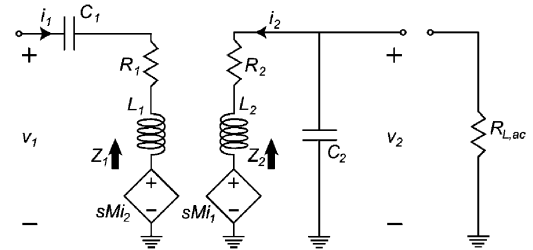

Fig. 2.   Inductively coupled series-parallel resonators. Coupling between the inductors is modelled with dependent voltage sources sMi_1 and sMi_2.

that demonstrates sufficiently small loss for a load power of 1 mW such that high overall energy efficiency in an RF link is achieved. Our overall efficiency measurements also include losses due to rectifier circuits.

This paper is organized as follows. In Section II, we discuss the theory of linear coupled resonators, the role of feedback, and derive expressions for efficiency. In Section III, we discuss the design of a bionic implant power system, with attention to efficiency at low power levels. In Section IV, we present experimental results. In Section V, we conclude by summarizing the main contributions of this paper.

II. BASIC MODEL OF COUPLED RESONATORS IN AN RF LINK

A pair of magnetically coupled resonators are shown in Fig. 2 and represent a model of our RF link with the primary resonator on the left and the secondary resonator on the right. The mutual inductance between the primary and secondary is represented by M. The resistances R_1 and R_2 are implicit resistances due to coil losses in the inductances L_1 and L_2 while C_1 and C_2 are explicit capacitances used to create a resonance in the primary and secondary, respectively. Using a resonant secondary circuit amplifies the induced voltage and is helpful in overcoming the turn-on voltage of rectifier diodes. A series-resonant primary network requires lower voltage swings at its input because the phase of the inductor and capacitor voltage cancel at resonance.

The rectifier circuit that is in parallel with C_2 has been replaced by an equivalent linear resistance $R_{L,ac}$ that represents its effect at the RF frequency. If the ripple on the output of the rectifier circuit is small, achieved due to a large load capacitance C_{RECT} at its output as shown in Fig. 1, then, since the rectifier output dc voltage is approximately the peak ac RF voltage at C_2, the ac rms energy at RF must be equal to the dc energy dissipated at the resistor by energy conservation; thus, $R_{L,ac} = R_L/2$,
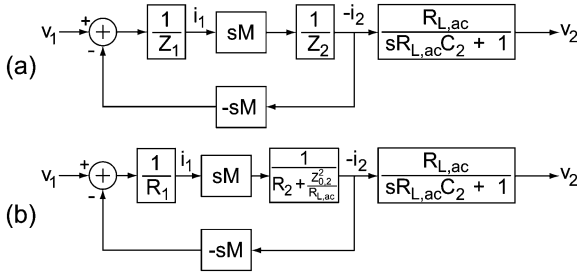
Fig. 3. Feedback diagrams for coupled resonators in Fig. 2. (a) Loop diagram under all frequencies. (b) Approximate loop diagram under resonant conditions $\omega = 1/\sqrt{L_1 C_1} = 1/\sqrt{L_2 C_2}$.
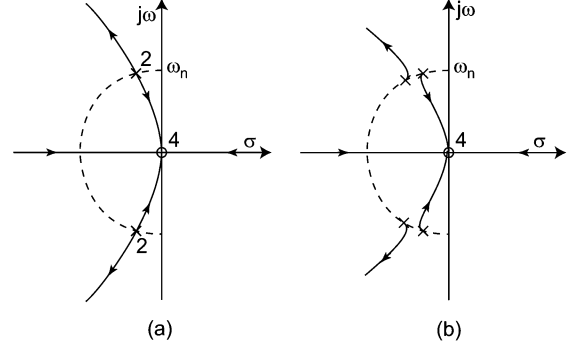

Fig. 4. Root locus diagrams are shown for two resonator cases. (a) Resonators are identical. A loaded resonator case (b) will have a higher damping factor due to energy lost to the rectifier. In this case the poles move together before splitting from the constant-ω_n circle.

where R_L is the effective load of all the internal implanted circuits powered by the rectifier supply created at C_{RECT}.

The geometric coupling factor between two coils of wire k is the ratio of common flux linkage between the coils. If two coils of wire are placed near each other, the common flux between the two coils cannot exceed the total flux produced by either of the coils. Therefore, for a uniform dielectric environment the coupling factor $|k| < 1$. Writing the mutual inductance as the geometric product of the discrete inductances $M = k\sqrt{L_1 L_2}$, we can also understand the coupling factor k as the fraction of induced voltage on one coil due to current in the other coil. We model this dependency with the controlled sources sMi_1, and sMi_2 in our coupled resonators.

A. Feedback Analysis

The block diagram in Fig. 3(a) models the circuit of Fig. 2. The loop transmission

$$L(s) = \frac{s^2 M^2}{Z_1(s) Z_2(s)} \tag{1}$$

$$L(j\omega) = \frac{-\omega^2 k^2 L_1 L_2}{Z_1(j\omega) Z_2(j\omega)} \tag{2}$$

is of a form that appears to indicate positive feedback at dc. The loop transmission $L(j\omega)$ near $\omega = 0$ is $k^2 \omega^4 L_1 C_1 L_2 C_2$ implying a positive loop transmission at and near dc. While this may seem puzzling at first, the loop transmission is easily interpreted as the product of two Lenz's law expressions, each of which implements negative feedback from one coil to another, but whose product is positive. The magnitude of the loop transmission at $\omega = 0$ is 0 and at $\omega = \infty$ is k^2, which is less than 1. The phase and magnitude of the feedback changes with frequency in between these limits according to the expressions above.

The feedback effects can be viewed as creating an effective impedance in the primary circuit due to reflected impedance from the secondary if we evaluate sMi_2/i_1. Using our feedback diagram

$$\frac{sMi_2}{i_1} = -\frac{s^2 M^2}{Z_2} = -Z_1 L(s). \tag{3}$$

Looking into the input of the primary resonator, the net input impedance Z_{in} is then given by

$$Z_{\text{in}}(s) = Z_1(s)(1 - L(s)). \tag{4}$$

As the coupling increases the loop transmission, the input impedance is dominated, first by the primary impedance $Z_1(s)$ and then by the impedance seen in the primary due to reflected secondary loading $-Z_1(s)L(s)$. The feedback block diagram in Fig. 3(b) shows a simplification of the block diagram under resonant conditions when $\omega_n \approx 1/\sqrt{L_1 C_1} \approx 1/\sqrt{L_2 C_2}$ where $Z_{0,2}{}^2/R_{L,ac} = L_2/R_{L,ac}C_2$ is the parallel-to-series impedance transformation of $R_{L,ac}$ due to the resonator formed by L_2 and C_2.

B. Root Locus Analysis

A helpful simplification to the loop transmission in the feedback loop in Fig. 3(a) is to write the resonators as second-order systems with quality factor Q and natural frequency ω_n

$$Z = \frac{s^2 + \frac{sR'}{L} + \frac{1}{LC}}{\frac{s}{L}} = \frac{s^2 + s\frac{\omega_n}{Q} + \omega_n^2}{\frac{s}{L}} \tag{5}$$

where R' is the effective resistance due to all losses in the primary or secondary. Finding the simplified loop transmission using the bandpass definitions in (5), we get

$$L(s) = \frac{s^2 M^2}{Z_1 Z_2} = \frac{s^2 k^2 L_1 L_2}{Z_1 Z_2}$$
$$\simeq \frac{k^2 \frac{s^2}{\omega_{n,1}^2} \frac{s^2}{\omega_{n,2}^2}}{\left(\frac{s^2}{\omega_{n,1}^2} + \frac{s}{\omega_{n,1} Q_1} + 1\right)\left(\frac{s^2}{\omega_{n,2}^2} + \frac{s}{\omega_{n,2} Q_2} + 1\right)}. \tag{6}$$

Here, the natural frequencies of the resonators are $\omega_{n,1}$ and $\omega_{n,2}$, respectively.

Under feedback, the open-loop poles associated with each of the resonators move on the complex plane as the geometric coupling factor k varies with inter-coil separation or misalignment and changes the root-locus gain. In a retinal implant the eye moves during normal patient activity changing k. Each of the resonators in Fig. 2 is characterized by a natural frequency, ω_n, and damping factor, $\zeta = 1/2Q = R/2\omega L$. Ideally, the quality factor of each resonator is set by only the effective coil resistances, R_1 and R_2, and $R_{L,ac}$; however, in a real system, the resistance of the power amplifier, resistance in the capacitors and objects in the environment can all contribute to reducing the effective quality factor of the coils.
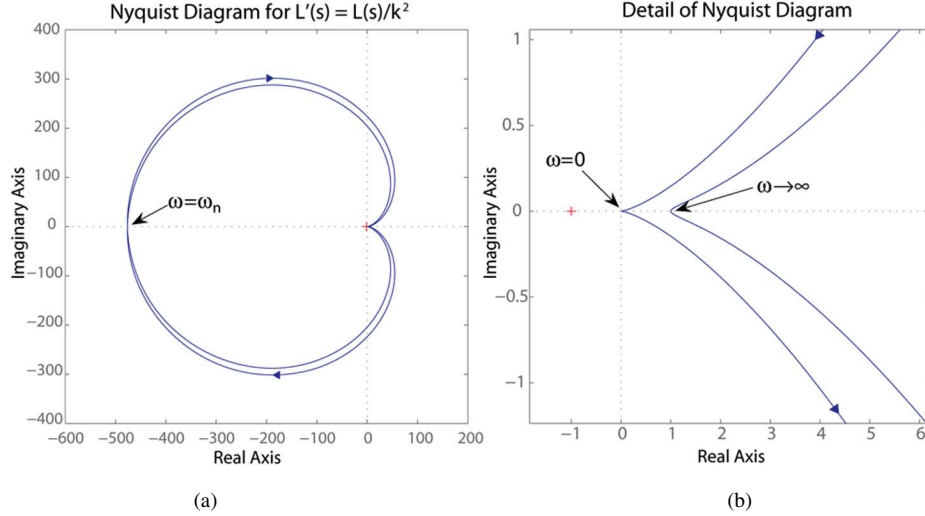
Fig. 5. Overall Nyquist diagram of $L(s)/k^2$ is shown in (a) and detail near the origin is shown in (b). As the frequency approaches ω_n the Nyquist plot approaches the $180°$ point with magnitude $Q_1 Q_2'$. For $L(s) = -1$, and this phase condition we must have $k = k_c$.

Fig. 4 shows how the four open-loop complex poles move under positive feedback as the root-locus gain parameter k^2 is changed. The techniques used to create this plot are the standard techniques of root locus from feedback theory [10]. The open-loop poles in Fig. 4(a) are identical and model the case where no loading is applied to the secondary circuit. Now, if we add the resistor $R_{L,ac}$ to model rectifier loading, the damping of the secondary resonators will be different from that of the primary. The open-loop secondary poles appear more damped on the ω_n circle, shown in Fig. 4(b). In this new configuration the poles move along the ω_n circle towards one another and then split along the trajectory loci for the unloaded case. The four asymptotes of the root-locus trajectories enter the origin along the positive and negative X axis and positive and negative Y axis asymptotes at infinite root-locus gain. It is interesting to note that the root-locus trajectories predict that the lower frequency closed-loop pole pair that is radially closer to the origin and moving towards it will have a higher quality factor due to their extreme angle of entry, while the closed-loop pole pair that is radially further from the origin and moving away from it will have a lower quality factor due to their less extreme angle of entry. Our experimental measurements, presented in Fig. 7(a) in a future portion of the paper, confirm this theoretical prediction, a fact that is seen in all prior data in the literature, but that appears to have never been commented on or explained.

C. Coupled Resonator Voltage Transfer Function

From the block diagram in Fig. 3, we can write the transfer function

$$
\begin{aligned}
\frac{v_2(s)}{v_1(s)} &= \left(\frac{L(s)}{1 - L(s)} \right) \left(\frac{1}{sM} \right) \left(\frac{R_L}{sC_2 R_L + 1} \right) \\
&= \left(\frac{L(s)}{1 - L(s)} \right) \left(\frac{1}{sk\sqrt{L_1 L_2}} \right) \left(\frac{R_L}{sC_2 R_L + 1} \right) \\
&= \left(\frac{kL'(s)}{1 - k^2 L'(s)} \right) \left(\frac{1}{s\sqrt{L_1 L_2}} \right) \left(\frac{R_L}{sC_2 R_L + 1} \right) \quad (7)
\end{aligned}
$$

where we have defined $L(s) = k^2 L'(s)$ to explicitly indicate the dependence of the loop transmission on the parameter k. By differentiating the latter equation w.r.t. k and equating it to zero, it's easy to show that the voltage transfer function has an extremum when $k^2 L'(s) = -1$, i.e., when the loop transmission $L(s)$ is -1. Physically, this extremum can be shown to be a maximum: When k is small, the voltage transfer function is small because there is little coupling of the current in the primary to the dependent voltage source in the secondary; when k is large, the input impedance seen in the primary $Z_{in}(s) = Z_1(s)(1 - L(s))$ increases as $L(s) = k^2 L'(s)$ increases with k such that the current in the primary reduces, decreasing the voltage transfer function. The optimal or critical coupling occurs when $k^2 L'(s) = L(s) = -1$, at which point the voltage transfer function is maximized. At this value of $k = k_c$, the link is said to be critically coupled. Note that at this value $Z_{in}(s) = 2Z_1(s)$ or equivalently, the reflected impedance of the secondary in the primary, $-Z_1(s)L(s)$, is equal to $Z_1(s)$.

At resonance, the loop transmission can be further simplified by including the effect of the load resistance, $R_{L,ac}$, transformed by the secondary circuit

$$
L(s)\big|_{\omega_n} = -k^2 \left(\frac{\omega L_1}{R_1} \right) \left(\frac{\omega L_2}{R_2 + \frac{Z_{0,2}^2}{R_{L,ac}}} \right) = -k^2 Q_1 Q_2'. \quad (8)
$$

where Q_2' is the loaded Q of the secondary and implicitly defined as shown. Thus, at critical coupling

$$
k = k_c = \frac{1}{\sqrt{Q_1 Q_2'}}. \quad (9)
$$

At this critical coupling, since the reflected resistive impedance of the secondary in the primary is equal to the resistive impedance in the primary, 50% of the power of the primary driver is dissipated in the secondary. Thus, the maximum energy efficiency at critical coupling is 50%. The actual energy

TABLE I
EFFICIENCY TEST SETUP PARAMETERS

Parameter	Notes
Output Power Level $P_{R_{L,ac}}$	4mW
Operating Frequency f	$\simeq 4.5$MHz
Coil Separation Distance d	$1mm - 30mm$
Class-E Power nFET	Fairchild NDS351
	$R_{DS,on} \simeq 0.6\Omega$ for $V_{GS,on} = 3V$
L_1	10 turns of 32 gauge $r = 15mm$
	3.2μH with $Q_1 \simeq 70$
C_1	150pF
C_S	60pF
L_2	15 turns of 32 gauge $r = 15mm$
	4μH with $Q_2 \simeq 70$
C_2	220pF
L_{RFC}	Coilcraft 1812PS-223KL
	$L_{RFC} = 22\mu$H

efficiency is lower than 50% because all of the energy dissipated in the secondary is not dissipated in the load $R_{L,ac}$ but some of it is dissipated in the coil resistance R_2 as well.

The Nyquist plot of $L'(s) = L(s)/k^2$ is shown in Fig. 5 such that $1/k^2$ may be viewed as a gain parameter of the plot. Since k^2 is always less than 1, the $1/k^2$ point always lies outside the contour that intersects the "1" point, therefore, in this positive-feedback version of the classic Nyquist plot, stability is guaranteed. Note, that at the $180°$ phase point, each resonator contributes approximately $90°$ of phase at its natural frequency $\omega_{n,1} \approx \omega_{n,2} \approx \omega_n$. The critical coupling point, being a maximum, yields robustness in the primary-secondary voltage gain to variations in intercoil distance or misalignment, which affect k.

D. Limits to Energy Efficiency

As energy flows from the source v_1 to the load element $R_{L,ac}$, it is diverted or dissipated in two mechanisms. First, energy must couple from the primary circuit to the secondary circuit and this coupling depends on the reflected load of the secondary in the primary. Second, energy in the secondary circuit dissipates either in the load element $R_{L,ac}$ or in the lossy resonator element R_2. The secondary circuit is most efficient when operated at resonance $\omega_{n,2} = 1/\sqrt{L_2 C_2}$. Choosing the primary circuit with the same series resonance increases the voltage gain between the primary and secondary and minimizes the input voltage at the primary.

1) Primary-Secondary Energy Transfer: Energy delivered to the primary circuit is either dissipated in the intrinsic resistance R_1 or delivered to the secondary. Of course, this statement ignores any loss mechanisms which may be present in the surrounding medium. Driving the dependent source impedance represents the work required to deliver power to the secondary circuit. Thus, the fraction of power transferred to the secondary circuit is the split between power in the intrinsic resistance R_1 or the dependent source sMi_2. From our feedback diagram, we can write the reflected impedance in the dependent source

$$Z_{2,1} = \frac{sMi_2}{i_1} = \frac{\omega^2 M^2}{\left(R_2 + \frac{Z_{0,2}^2}{R_L}\right)}. \qquad (10)$$
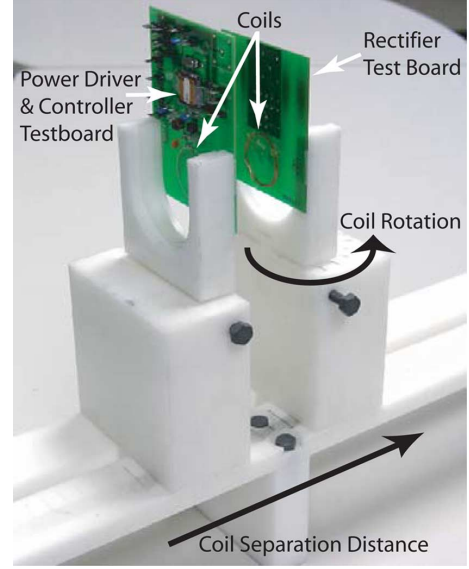

Fig. 6. Test setup used for inductive power transfer system tests is shown. The coil separation can be adjusted and measured with millimeter accuracy. Coil rotation can also be explored for both the primary and secondary coils. The electronic boards are glued to Delrin scaffolding with Teflon screws used to bind the various portions of the scaffold.

The same current i_1 flows through both elements, and we can write the fraction of energy dissipated in the dependent source as a voltage divider using (3), (4), and (8)

$$\eta_k = \frac{P_{sMi_2}}{P_{IN}} = \frac{i_1^2 Z_{2,1}}{i_1^2 Z_1 + i_1^2 Z_{2,1}}$$
$$= \frac{Z_1 L(s)}{Z_1 - Z_1 L(s)} = \frac{k^2 Q_1 Q_2'}{1 + k^2 Q_1 Q_2'}. \qquad (11)$$

Typically, the unloaded secondary circuit can have a high quality factor meaning that overall quality factor Q_2' is dominated by the quality factor of the load $Q_L = \omega R_L C_2$. Equation (11) indicates the need to maximize the geometric coupling factor k, quality factor of the primary circuit Q_1, and the loaded quality factor of the secondary circuit Q_2', to achieve minimum dissipation in the primary coil's resistance. The equation also illustrates that above the critical coupling factor k_{crit}, the primary-secondary coupling efficiency increases from 0.5 and begins to approach 1. From the Nyquist diagram for $L'(s)$ in Fig. 5, we see that the maximum value of $|L'(s)|$ is $Q_1 Q_2'$. At this maximum point, we can operate at or above $k = k_c$ to have a coupling efficiency between the primary and secondary greater than 50%.

2) Energy Dissipation in the Secondary Circuit: The energy coupled to the secondary circuit is dissipated in both the parasitic element R_2 and the load network, represented in this linear model by $R_{L,ac}$. At resonance, writing the fraction of power delivered to the load element

$$\eta_2 = \frac{P_L}{P_2} = \frac{Q_2}{Q_2 + Q_L}. \qquad (12)$$

Equation (12) represents the energy divider relationship during the waveform cycle between the lossy elements R_2 and $R_{L,ac}$. Equation (12) delivers maximum energy to the load when the effective Q of the load network $Q_L = \omega R_{L,ac} C_2$, is minimized.
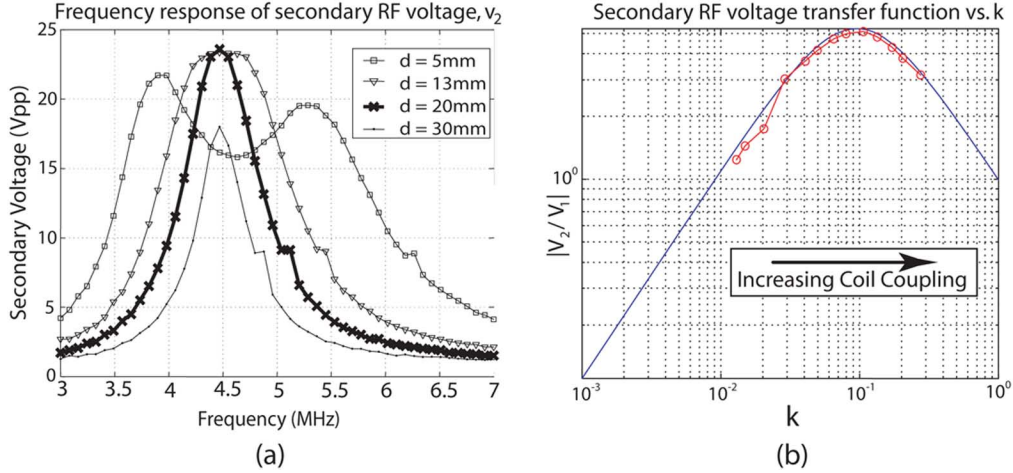
Fig. 7. (a) Shows how the closed-loop poles move as the coil distance is changed. At some coil separation, the poles begin to move apart and a low-frequency high-Q and high-frequency low-Q peak are observed. (b) Shows the voltage peak at resonance as we change the coil coupling factor. The peak occurs at roughly $k_c \sim 0.1$.

From (11), the primary-secondary coupling efficiency η_k increases as Q_L is increased since $Q_2' = (Q_2 Q_L / (Q_2 + Q_L))$; from (12), the secondary efficiency decreases as Q_L is increased. Thus, there is an optimum Q_L or equivalently, an optimal load $R_{L,ac}$, at which the overall energy efficiency is optimized.

3) Optimal Loading Condition: The net energy efficiency is given by

$$\eta_2 \eta_k = \left(\frac{k^2 Q_1 Q_2'}{1 + k^2 Q_1 Q_2'} \right) \left(\frac{Q_2}{Q_2 + Q_L} \right). \tag{13}$$

By differentiating (13) w.r.t. Q_L, we find an optimal loading condition at which the energy efficiency is maximized

$$Q_{L,\text{opt}} = \frac{1}{k} \sqrt{\frac{Q_2}{Q_1}}. \tag{14}$$

At this optimum, the maximum achievable efficiency can be written in terms of the coupling factor and unloaded quality factors of the coils, Q_1 and Q_2

$$\eta_{\text{MAX}} = \frac{k^2 Q_1 Q_2}{(k Q_1 + 1)(k Q_2 + 1)}. \tag{15}$$

This form is more practical than writing a full solution of the losses in each resistive element and summing them as has been done previously [6].

Using values of experimental components listed in Table I, and the experimental setup shown in Fig. 6 and described in its caption, we obtained measurements of our RF link that illustrate the theoretical effects that we have been discussing. Fig. 7(a) reveals the frequency transfer functions of coupled resonators as the distance between the primary and secondary is varied. We note that after the critical coupling distance (or equivalently after the critical coupling k_c), where the voltage transfer function is maximized, there are two frequency peaks with the lower frequency peak having higher Q and the higher frequency peak having lower Q in accord with the root-locus predictions of Fig. 4. Fig. 7(b) shows that the voltage peak at resonance is non-monotonic and peaks at the critical coupling
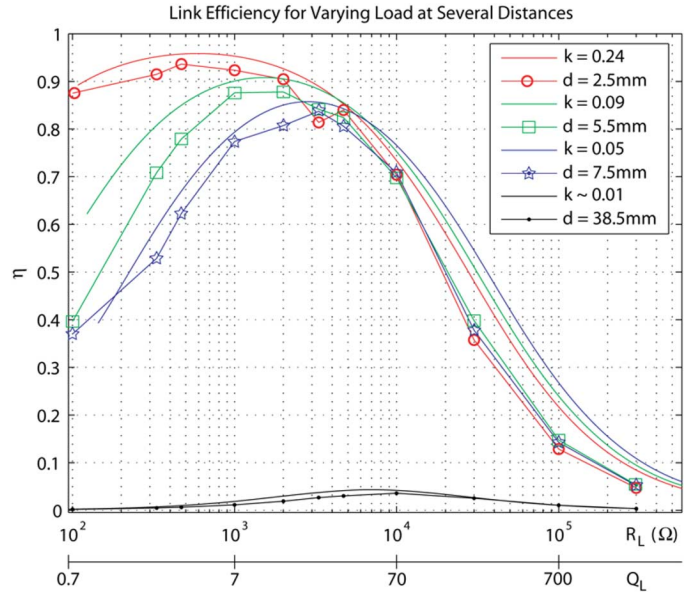

Fig. 8. Efficiency of power transfer between coupled resonators for varying loading. The data we show were produced by ignoring switching losses in a discrete Class-E amplifier implementation.

$k_c \approx 0.1$. Fig. 8 shows the results of the overall power transfer efficiency (ignoring the Class-E amplifier and rectifiers for now) for four separation distances. Note that the peak efficiency shifts to lower load resistance as the coils are moved closer together in accord with the theoretical predictions of (14).

III. SYSTEM DESIGN

The power driver, inductive link, secondary circuit, and rectifier, each contribute to wasted power. The overall efficiency of the power system is the product of the power-processing stages, including the driver efficiency η_{driver} and the rectifier efficiency η_{rect}. The overall efficiency is just the effect of all of these stages on the input power $\eta_{\text{total}} = \eta_{\text{driver}} \eta_k \eta_2 \eta_{\text{rect}}$.

Equation (15) predicts that the best unloaded quality factor for both primary and secondary coils maximizes the asymptotic

efficiency of the link. Coils generally have better Q at higher frequency ω since their electromagnetic skin-effect resistive losses scale like $\sqrt{\omega}$ while their reactance scales like ω. A large operating frequency does however, lead to more sensitivity to parasitics, increased tissue absorption, and increased losses and or increased power in the Class-E drivers that require better timing precision at higher operating frequencies. The presence of the high dielectric tissue of the body surrounding the implant can also lower the self-resonance frequency of the coil due to inter-turn coupling. With these tradeoffs in mind, we chose to operate at 6.78 MHz, an unlicensed ISM band. We used multistranded Litz wire for the coils. Such wire mitigates skin-loss resistive effects by accumulating the increased skin-effect circumferential area available in each strand of wire rather than relying on the skin-effect circumferential area available in just one strand. In this operating frequency band, we obtain inductors from 1 to 15 μH and quality factors of 80–150. More details on the influence of the number of turns, coil separation, and coil misalignment on k can be found in [11].

Our design procedure begins with the inductive link and secondary circuit, as these are typically the most difficult to maximize. Then the design of the power driver and rectifier follow. Our design is based on the following steps.

1) From the given load that one is required to drive in the secondary, and the mean expected k, design the secondary circuit for achieving optimal overall efficiency from (14) and (15), and to maintain resonance at the desired operating frequency.

2) Choose a desired primary-secondary voltage gain of the link and implement it by choosing appropriate element values in the primary.

3) Design the power driver and rectifier circuits to be as efficient as possible by optimizing their design to yield minimum loss.

A. Resonator Design—Load Design

From the limitations on the physical size of the implanted and external coils, we can find the range of coupling factors for the operation of the system. The range of coupling factors can be reduced with intentionally misaligned coils [12], at the expense of peak efficiency. In many transcutaneous bionic implants, the skin-flap thickness, d, can vary from 1 to 10 mm. The implanted and external coils are chosen to have a radius of 14 mm. This size and range of separations gives a range of coupling factors $0.04 < k < 0.17$. As the 6-mm condition is the most common, we have chosen the coupling factor of 0.084 as our optimal coupling factor. Therefore, the optimal loading quality factor is $Q_{L,\text{opt}} \simeq 12$.

Our electrode stimulation circuits present an effective load resistance to each of the rectified supply voltage nodes $+V_{\text{RECT}}$ and $-V_{\text{RECT}}$ of 10 kΩ. For both rectifiers in parallel, the effective ac resistance load $R_{L,ac} = 2.5$ kΩ. Now, with the operating frequency and the load quality factor chosen, this constrains the choice of secondary capacitance and inductance. Note that the effective capacitance at the resonator node, v_2, must account for the capacitance due to the diodes, as well as parasitic capacitance due to the self-resonance of the coil. For a robust implanted design, the coil capacitance must be much smaller than

TABLE II
SECONDARY RESONATOR DESIGN

Parameter	Notes
$R_{L,ac}$	2.5kΩ
C_2	93pF Mica $Q \sim 400$
Rectifier Diode, D	2 $\times$ HBAT54C Schottky diode $C_{par} \simeq 13pF$
$C_{2,total}$	119pF
L_2	8 turns of 22-strand Litz wire $r = 15mm$ 4.7μH with $Q \sim 140$
Unloaded Q_2	90
Q_L	12.6

the explicit capacitance at the node C_2, to prevent tuning shifts when the unit is implanted under tissue. Our final secondary circuit design is summarized in Table II.

With the secondary network chosen, we can turn to the design of the primary. The voltage gain between the primary and secondary circuits can be scaled by choosing the primary inductance L_1 w.r.t. the secondary inductance L_2. The voltage gain at the critical coupling when $k_{crit}^2 |L(j\omega_n)| = 1$ is the maximum possible gain obtainable. Its value is easily found by substituting $M = k_{crit}\sqrt{L_1 L_2}$, $k_{crit}^2 Q_1 Q_2' = 1$, $L_1 C_1 = L_2 C_2 = 1/\omega_n^2$, and $L(s) = -1$ in (7) with $\omega_n C_2$ assumed much greater than $1/R_{L,ac}$ (i.e., Q_L is at least greater than 10). It is found to be

$$\left(\frac{v_2}{v_1}\right)_{\text{MAX}} = \frac{\sqrt{Q_1 Q_2'}}{2}\sqrt{\frac{L_2}{L_1}}. \tag{16}$$

For our system, we chose a primary inductance of $L_1 = 6.5\,\mu$H to reduce the gain due to the high quality factor of our resonators. With the choice of L_1, the value of C_1 is chosen such that L_1 and C_1 resonate at ω_n.

B. Driver Design

When designing power amplifiers to drive the primary in low-power RF links, there are three considerations: First, the output resistance of the drive circuitry must not reduce the effective quality factor of the primary circuit greatly to maintain the asymptotic efficiency performance derived in (15). Second, the driver should be resilient to changes in the load—the reflected load from the secondary circuit can constantly change the primary resonator's damping characteristics. Finally, complex techniques for reducing capacitance switching at control terminals in a power amplifier are too costly in milliwatt systems like ours and are to be avoided. A design that fulfills these requirements is described below.

Fig. 9 shows a Class-E power amplifier. A single switch M is used to periodically toggle between fluxing up an inductor L_{RFC} or switching the current in the inductor to the output network at the drain node v_d. The resultant square wave harmonics are filtered by the resonant driven network. With careful choosing of the load C_S w.r.t. to the dynamics and parameters of the driven primary network, this topology can minimize $f C_S v_d^2$ switching losses in M, by only turning M on when v_d is near ground [13].

The damping seen in the driven primary changes due to variations in the reflected impedance from the secondary caused by variations in coupling. To adapt to these changes, we built a simple one-shot feedback controller, shown as control blocks
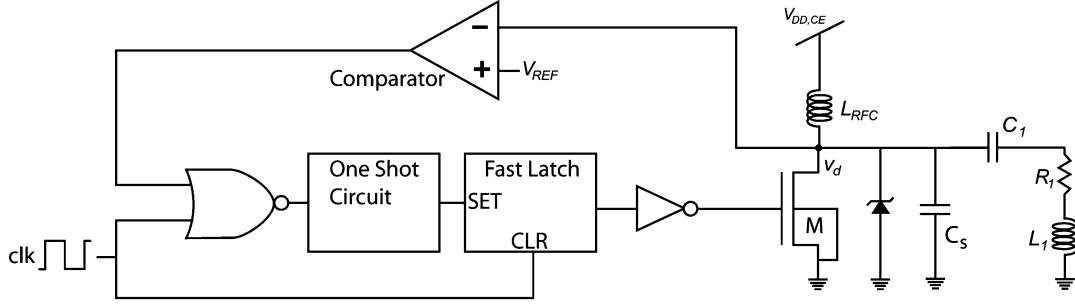
Fig. 9. Switching power driver (Class-E) is shown with the primary circuit and a one-shot control loop. The Class-E supply voltage $V_{DD,CE}$ controls the power level, while the clock, comparator, NOR gate, one-shot circuit, and latch control the gate drive timing.
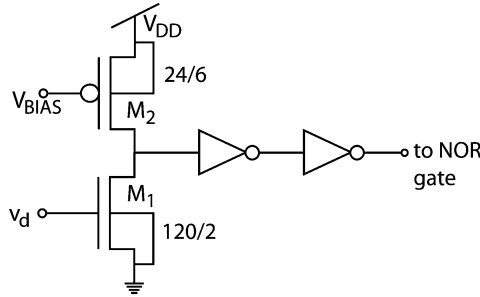

Fig. 10. Simple comparator for the Class-E controller. The comparator triggers the NOR gate when v_d approaches zero volts. The device sizes were ratioed to obtain a low voltage threshold. The threshold is intentionally not exactly at ground to allow for some error compensation due to delays in our control scheme.

on the left half of Fig. 9. Our drive circuit is triggered by a fixed clock which resets the gate drive signal through a dynamic latch turning the power switch M off when the clock goes low. The current from L_{RFC} is then directed onto C_S and the primary network. When the resonator voltage drops near ground again due to the resonant behavior of the driven network the comparator triggers and turns on the power switch through the NOR gate, a pulsatile one-shot, and fast latch. If the comparator signal has not arrived by the end of the clock cycle, then the high-going clock will turn on M. Thus, the controller achieves fixed-frequency operation set by the clock, but adapts to changes in the driven network that speed up the return of v_d to ground. The comparator is implemented as a simple ratioed inverter and shown in Fig. 10.

1) Optimal Device Sizing of the Switching Transistor in the Class-E Amplifier: When the switching transistor M in Fig. 9 is turned on, it conducts current flowing from L_{RFC} and from the primary resonator. A large W/L for the switching transistor M in Fig. 9 reduces its on resistance, $R_{DS,on}$. A low $R_{DS,on}$ is important for ensuring that the quality factor of the driven primary resonator is not degraded greatly; a large W/L also minimizes the $I_{RFC}^2 R_{DS,on}$ loss, although this loss is rather small in our design. However, a large W/L in the M device increases the the input gate capacitance of M and begins to increase switching losses at its gate input. Thus, there is an optimal W/L sizing that minimizes the power losses in M due to gate switching and due to increased losses in the primary resonator.

To estimate this optimum, we shall first assume that Q_1 in the primary resonator circuit is determined entirely by $R_{DS,on}$ since it was found to be significant compared with R_1 in our design. Then, from (11), with $Q_1 = (\omega_n L_1)/R_{DS,on}$ and $Q_2' \approx Q_L$, we get

$$P_{R_{DS,on}} \simeq \frac{P_{IN}}{1 + k^2 Q_L \frac{\omega L_1}{R_{DS,on}}}. \tag{17}$$

Equation (17) yields the resonator power loss as a function of $R_{DS,on}$ or equivalently with $1/(W/L)$ of the transistor M. If we sum this power loss with the increase in gate switching power, which rises with WL in the transistor, we can find an optimum. The optimum in our 0.5 μm process is near 1200 μm × 0.5 μm. Such a transistor is implemented with many parallel fingers on a chip.

During the time when the FET M is turned off, the drain voltage pulse can reach high voltage values. Our integrated devices have a breakdown voltage of 11 V. To avoid breaking down these devices, the resistance seen in the primary by the Class-E driver must be low enough to not cause breakdown or we must run the Class-E driver with $V_{DD,CE}$ in Fig. 9 low enough to not cause breakdown. In addition, an off-chip Schottky diode protects v_d from under voltages below ground. At our low power levels, the effective magnetic field strength is low enough such that regulatory issues are not a big concern.

IV. Measured Performance

We fabricated a power-system chip on AMI's 0.5-μm SCMOS process offered by MOSIS. Fig. 11 shows the die which includes two sizes of power switches, and includes independent gate drivers and controllers, PTAT comparator biasing, a crystal clock generator, and a feed-forward data path (not described in this paper). Testing was done for a 1.8-V digital supply voltage. The controller comparator, shown in Fig. 10, was biased with 28 μA and sized to minimize delay. Including wasted biasing power, the comparator consumes 56 μW of power. The gate driver and remaining control circuits consume 48 μW from the supply. All these dissipations are added in our computations of the final efficiency so that it is as accurate is possible. Table III shows our final measured parameters for the rest of the system.
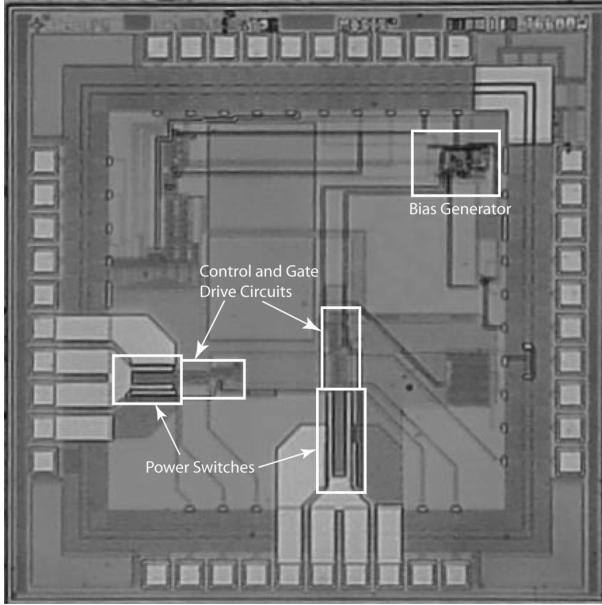
Fig. 11. Die photograph of the 0.5-μm power systems chip. This chip includes two power switches and two independent controllers. A clock generator, for off-chip crystals, as well as a feed-forward data system (not discussed in this paper) are also included on the chip.

TABLE III
FINAL SYSTEM SPECIFICATIONS

Parameter	Notes
Output Power Level, $P_{R_{L},dc}$	1mW – 10mW
	$+V_{RECT}, -V_{RECT}$
	with $R_{L,dc} = 10k\Omega$ each
Operating Frequency, f	6.785MHz
Coil Separation Distance d	$1mm - 10mm$
Class-E nFET	100 fingers $\times 12\mu m \times 0.5\mu m$
	$C_{gate} \sim 2.1pF$
Class-E Supply Voltage, $V_{DD,CE}$	0.6V – 2.5V
L_1	22-strand Litz wire $r = 15mm$
	10 turns 6.5μH with $Q_1 \sim 94$
C_1	1000pF Mica
C_S	30pF
L_2	22-strand Litz wire $r = 15mm$
	8 turns 4.7μH with $Q_2 \sim 90$
C_2	93pF
Rectifier Diode, D	2 $\times$ HBAT54C Schottky diode
	$C_{par} \simeq 13pF$
L_{RFC}	Coilcraft 1812PS-223KL
	$L_{RFC} = 22\mu$H

Our primary coil L_1 had an intrinsic quality factor of over 100. However, the power switch in the Class-E amplifier contributes to the effective series loss in the primary significantly, such that

$$Q_{1,\text{eff}} = \frac{\omega L_1}{R_1 + R_{\text{DS,on}}}. \tag{18}$$

Since $R_{\text{DS,on}}$ was found to be 5 Ω, it reduced the primary quality factor to 35. Table IV summarizes our final measured performance numbers including this effect. Fig. 12 shows the basic waveforms of our Class-E driver. Fig. 13 illustrates that our clocked one-shot strategy is operating over a 1-10-mm range of coil separations.

TABLE IV
FINAL SYSTEM PERFORMANCE

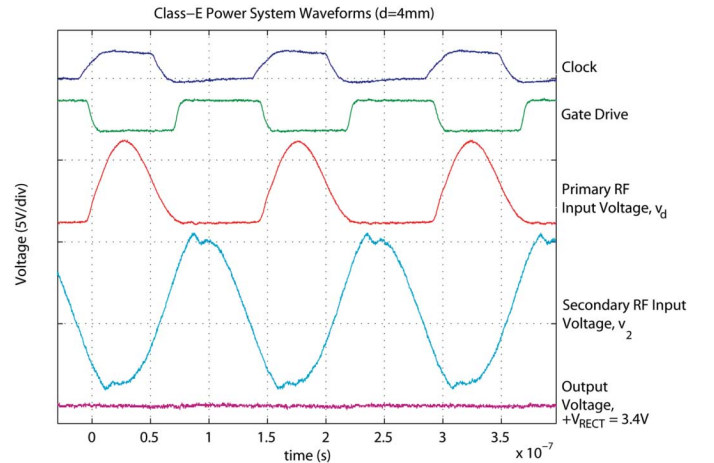| Component	Performance @ $V_{DD} = 1.8V$
Gate Driver	$46\mu W$
Gate Switching Controller	$56\mu W$
Power Switch, M	$R_{DS,on} \simeq 5\Omega$
$Q_{1,eff}$	35
Q_2	90
η_{total} @ 1mW	66% @ $d = 1mm$
	62% @ $d = 6mm$
	51% @ $d = 10mm$
η_{total} @ 10mW	74% @ $d = 1mm$
	66% @ $d = 6mm$
	54% @ $d = 10mm$

Fig. 12. System waveforms, including the clock, gate-driver signal, Class-E drain voltage v_d, secondary voltage v_2, and rectified voltage V_{RECT} are shown for a 4-mm coil separation condition.
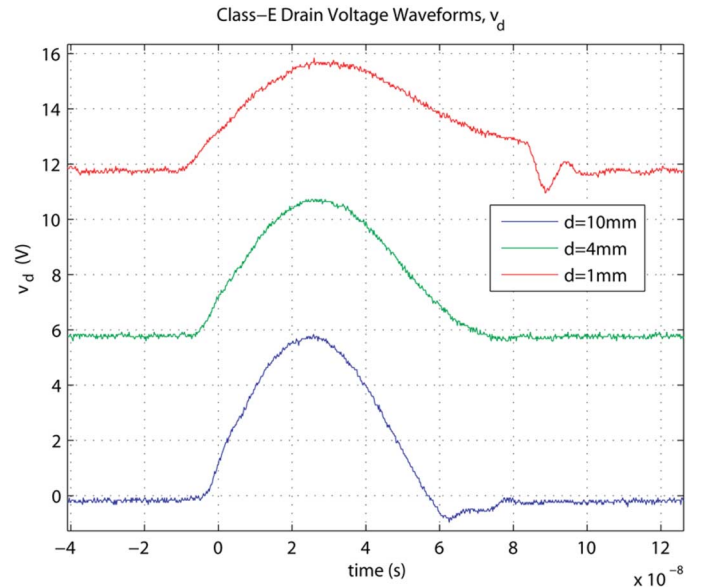

Fig. 13. Three cases are shown for the Class-E drain voltage v_d. Note that the switch timing has adapted slightly to reduce the amount of $fC_s v_d^2$ wasted power under the 1- and 10-mm conditions. Furthermore, the action of the protection diode can be seen in the $d = 10$ mm case where the drain voltage has dropped below ground.

Fig. 14 shows the variation of rectified output voltage over a range of coil separations. For all coupling cases, we have less
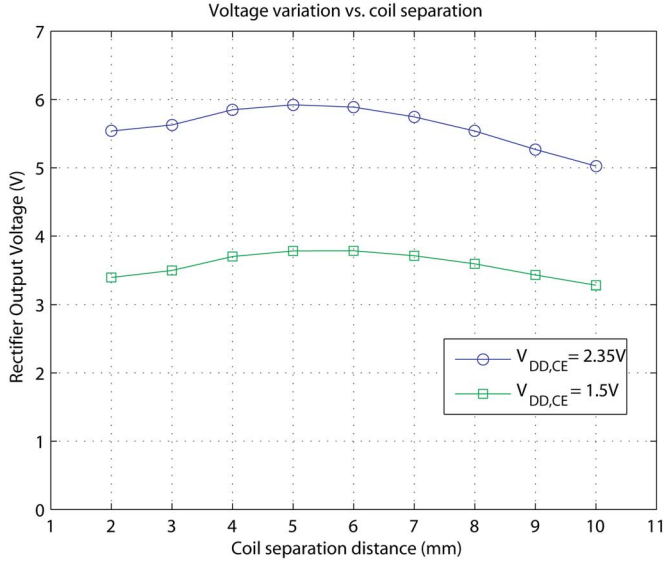
Fig. 14.   Variation in the rectified output voltage is shown for two power driver voltage levels. The rectified voltage variation is less than 16% for all cases.
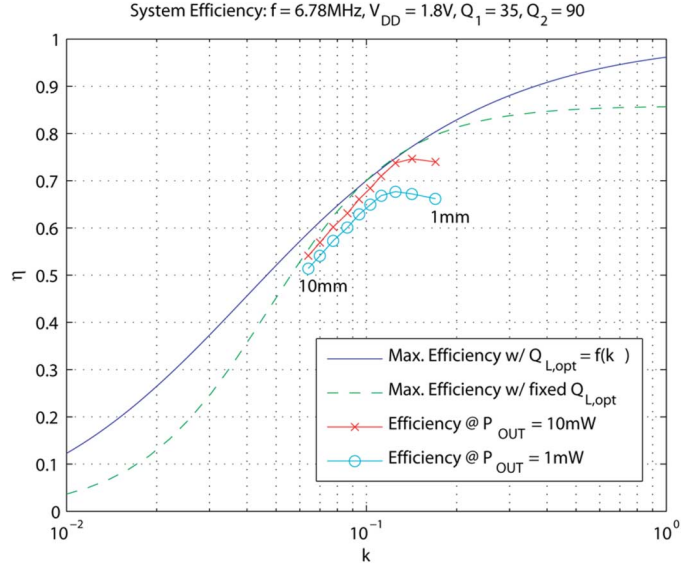

Fig. 15.   Comparison between the asymptotically efficient coupled resonator power transfer system ($Q_1 = 35$, $Q_2 = 90$) is shown with our system. The top curve indicates the maximum possible efficiency for an adapting load condition [see (15)]. The dashed theory curve indicates efficiency for our fixed loading condition $Q_{L,\mathrm{opt}}$ [see (13)]. Our system performance is shown for 10- and 1-mW operation.

than 16% difference in the minimum and maximum voltages. Thus, our design, which targets efficiency rather than critical coupling, is nevertheless robust in its voltage-transfer characteristic to changes in link coupling.

In future work, a feedback system which measures the appropriate primary–secondary voltage–power relationship can be implemented without much power. Such a system could use 4 bits to set the voltage range for the factor-of-10 variation in power levels from 1 to 10 mW. A range of primary class-E voltages from only 0.6 to 2.5 V can provide the needed range of power to the secondary over all possible separation conditions.

A. Efficiency

We tested the overall efficiency for a range of distances and power levels suitable for our application. Fig. 15 compares our measured efficiency with theoretical predictions. The top trace indicates the theoretical performance possible if the load is adapted for each coupling factor, i.e., (15). The dashed trace shows the theoretical performance for a fixed $Q_{L,\mathrm{opt}} \simeq 12$, our experimental situation, and for which (13) is predictive. As can be seen, the agreement with theory is fairly good. The 1-mW characteristic deviates more from theory than the 10-mW characteristic because the fixed power used by the controller and gate drive power are a more significant fraction of the overall power.

To examine deviations of experiment from theory more closely, Fig. 16 breaks down the efficiency of the various components of our system. These *efficiencies* were determined from measurements of the wasted power, the input power, and output power at the secondary. At the lowest power operating level, rectifier and gate-switching losses contribute the most because these losses do not scale with power level like efficiencies in linear portions of the system, e.g., the primary–secondary coupling.
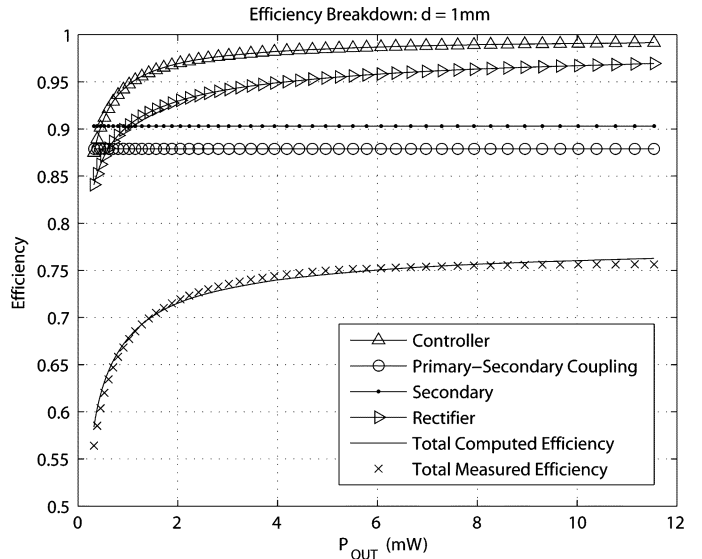

Fig. 16.   Plot of the efficiency is shown for a sweep in the power level by changing the class-E supply voltage. The efficiency of each mechanism is shown for comparison. At low power levels, controller power and losses in the rectifier contribute most to inefficiency of the system.

Our system delivers 10 mW at typical coil separations with 61% efficiencies, in excellent agreement with theoretical predictions. Note that a higher value of $Q_{L,\mathrm{opt}}$ would improve efficiency for low k as Fig. 15 shows or (14) predicts. The 5-Ω series resistance of our power switch degrades efficiency due to the reduction in the quality factor of the primary. If we use (15) at $k = 0.09$, and a redesigned value for $R_{\mathrm{DS,on}} = 2\ \Omega$, the asymptotic efficiency can be as high as 85%.

We obtained measurements with a bag of saltwater as well as a slab of Delrin between the primary and secondary coil. Our measurements indicated a slight shift in resonance frequency

which degraded our efficiency by 2%–3%. The robustness of our design to such effects is because an explicitly large C_2 in the secondary that dominates over stray capacitance and self-resonance effects in the coils.

V. CONCLUSION

We have used a feedback viewpoint to add geometric insight to the design of RF power links. Our design approach focused around the choice of an efficiency-maximizing load for an expected mean separation between primary and secondary coils. The approach also yields voltage-transfer functions that are fairly robust to changes in coil coupling parameters. We used these techniques to build an RF power link for use at 1–10-mW load power-consumption levels and for 1–10-mm coil separations. At such low power levels, rectifier losses and Class-E power amplifier losses contribute significantly to the inefficiency of the overall system. We described a novel integrated Class-E power amplifier design that used a simple control strategy to minimize such losses. At 10-mW load power consumption, we measured overall link efficiencies of 74% and 54% at 1- and 10-mm coil separations, respectively, in good agreement with our theoretical predictions of the link's efficiency. At 1-mW load power consumption, we measured link efficiencies of 67% and 51% at 1- and 10-mm coil separations, respectively, also in good accord with our theoretical predictions. In both cases, the link's rectified output dc voltage varied by less than 16% over link distances that ranged from 2 to 10 mm.

REFERENCES

[1] R. Sarpeshkar, C. D. Salthouse, J.-J. Sit, M. W. Baker, S. M. Zhak, T. K.-T. Lu, L. Turicchia, and S. Balster, "An ultra-low-power programmable bionic ear processor," *IEEE Trans Biomed. Eng.*, vol. 52, no. 4, pp. 711–727, Apr. 2005.

[2] R. Sarpeshkar, M. W. Baker, C. D. Salthouse, J.-J. Sit, L. Turicchia, and S. M. Zhak, "An analog bionic ear processor with zero-crossing detection," in *Proc. IEEE Int. Solid-State Circuits Conf.*, Feb. 2005, vol. 1, pp. 78–79.

[3] J.-J. Sit, A. M. Simonson, A. J. Oxenham, M. A. Faltys, and R. Sarpeshkar, "A low-power asynchronous interleaved sampling algorithm for cochlear implants that encodes envelope and phase information," *IEEE Trans. Biomed. Eng.*, to be published.

[4] G. A. Kendir, W. Liu, G. Wang, M. Sivaprakasam, R. Bashirullah, M. S. Humayun, and J. D. Weiland, "An optimal design methodology for inductive power link with class-E amplifier," *IEEE Trans. Circuits Syst. I, Reg. Papers*, vol. 52, no. 5, pp. 857–866, May 2005.

[5] P. R. Troyk and M. A. K. Schwan, "Closed-loop class-E transcutaneous power and data link for microimplants," *IEEE Trans. Biomed. Eng.*, vol. 39, no. 6, pp. 589–599, Jun. 1992.

[6] N. de N.Donaldson and T. A. Perkins, "Analysis of resonant coupled coils in the design of radio frequency transcutaneous links," *Med. Biol. Eng. Comput.*, vol. 21, no. 5, pp. 612–627, Sep. 1983.

[7] C. M. Zierhofer and E. S. Hochmair, "High-efficiency coupling-insensitive transcutaneous power and data transmission via an inductive link," *IEEE Trans. Biomed. Eng.*, vol. 37, no. 7, pp. 716–722, Jul. 1990.

[8] O. Omeni and C. Toumazou, "A CMOS micro-power wideband data/power transfer system for biomedical implants," in *Proc. IEEE 2003 Int. Symp. Circuits Syst.*, May 2003, vol. 5, pp. V61–V64.

[9] G. Wang, W. Liu, M. Sivaprakasam, and G. A. Kendir, "Design and analysis of an adaptive transcutaneous power telemetry for biomedical implants," *IEEE Trans. Circuits Systems I, Reg. Papers*, vol. 52, no. 10, pp. 2109–2117, Oct. 2005.

[10] G. Franklin, J. D. Powell, and A. Emami-Naeini, *Feedback Control of Dynamic Systems*, 5th ed.   Englewood Cliffs, NJ: Prentice-Hall, 2005.

[11] F. E. Terman, *Radio Engineers Handbook*.   New York: McGraw-Hill, 1943.

[12] C. M. Zierhofer and E. S. Hochmair, "Coil design for improved power transfer efficiency in inductive links," in *Proc. IEEE Eng. Med. Biol. Soc. 18th Annu. Int. Conf.*, 1996, pp. 1538–1539.

[13] N. O. Sokal and A. D. Sokal, "Class-E—A new class of high-efficiency tuned single-ended switching power amplifiers," *IEEE J. Solid-State Circuits*, vol. SSC–10, no. 2, pp. 168–176, Jun. 1975.

[14] C. Fernandez, O. Garcia, J. A. Cobos, and J. Uceda, "A simple dc-dc converter for the power supply of a cochlear implant," in *Proc. IEEE 34th Annu. Power Electron. Special. Conf.*, Jun. 2003, vol. 4, pp. 1965–1970.

Michael W. Baker (S'04) received the B.S. degree in electrical engineering and computer science and the M.Eng. degree on high-linearity mixers for 5-GHz receivers in 2000 and 2002, respectively, both from the Massachussets Institute of Technology (MIT), Cambridge, where he is currently working towards the Ph.D. degree in analog VLSI and biological systems.

His research interests include neural and bionic implants, low-power integrated analog design, and integrated radio-frequency circuits.

Rahul Sarpeshkar (M'01) received the B.S. degrees in electrical engineering and physics from the Massachussetts Institute of Technology (MIT), Cambridge, and the Ph.D. degree from the California Institute of Technology, Pasadena.

After receiving the Ph.D. degree, he joined Bell Laboratories as a member of the technical staff. Since 1999, he has been on the faculty of MIT's Electrical Engineering and Computer Science Department where he heads a research group on analog VLSI and biological systems, and is currently an Associate Professor. He holds over 20 patents and has authored several publications including one that was featured on the cover of *Nature*. His research interests include biologically inspired circuits and systems, biomedical systems, analog and mixed-signal VLSI, ultralow-power circuits and systems, neuroscience, molecular biology, and control theory.

Dr. Sarpeshkar has received several awards including the Packard Fellow award given to outstanding young faculty, the ONR Young Investigator Award, the Junior Bose Award for Excellence in Teaching at MIT, and the NSF Career Award.